

<https://doi.org/10.1038/s43247-025-02146-y>

Discrete fracture network modelling reconstructs fracture array evolution and related petrophysical properties over geological time

Check for updates

Matthew S. Hodge¹ , Mark Cottrell², Jochen Knies³ & Giulio Viola¹

Fractured rock petrophysical studies rarely use temporal constraints, thus hindering fracture-related permeability and connectivity estimation during past geofluid migration. Here we present a conceptual approach, using a stochastic method incorporating absolute ages to reconstruct fracture arrays back in geological time. Generating ‘grown’ discrete fracture network models, we simulate the hydraulic behaviour of fractured rock volumes from the late-Cretaceous/Palaeocene to the Devonian, via progressive fracture back-stripping. We reveal that for the examined rock mass, maximum principal permeability increased through time from $9.47\text{e-}14\text{ m}^2$ to $4.44\text{e-}13\text{ m}^2$ (~3 orders of magnitude) along with the maximum horizontal permeability orientation shifting from NE-SW to NW-SE. Similarly, the connectivity metric increased with fracture saturation, peaking in the mid-Cretaceous. For comparison, dated offshore hydrocarbon secondary migration potentially coincides with our results. Back-stripping of time-constrained fracture sets is therefore a powerful method to investigate and quantify the dynamic evolution of petrophysical properties through geological time.

Time constraints, such as the age of fracturing or veining, are seldom utilised in fractured media petrophysical studies (e.g. refs. 1–4) due to the general difficulty in deriving such constraints. In turn, the lack of absolute temporal information makes it challenging to constrain the chronological evolution of fracture-related petrophysical characteristics and to establish, for example, what role permeability and fracture connectivity played during past reservoir charging events. Applying time constraints to a well-studied fracture network may resolve which fracture sets, or combination thereof, afforded preferential fluid pathways at specific times. Furthermore, as geofluids may form and migrate episodically^{5,6}, the transient increase of fracture-related permeability (particularly in rocks with low matrix permeabilities) may be a key control on when and how fluid flow occurs. In addition to contributing to pure petrophysical studies, appreciating when higher secondary (‘paleo-’) permeability formed in a rock volume, and when meaningful fracture connectivity was established, can, in turn, provide crucial insights into the dynamics of reservoir charging and geofluid flow histories, thus crucially aiding geofluid exploration efforts and informing strategies for fluid storage project developments.

Old crystalline basement rocks become progressively saturated with fractures over time when experiencing extended polyphase deformation

(Fig. 1), with new fractures forming, or inherited fractures accommodating different deformational episodes^{7–9}. The addition of each new fracture set to a pre-existing fracture network may change how geofluids flow through a host rock¹⁰. Accordingly, a fractured rock volume today represents the sum of past configurations of fractures, chemical processes, petrophysical characteristics, and fluid flow states through geological time (Fig. 1). Unfortunately, the study of selected portions of this typically long history generally requires unravelling a seemingly chaotic array of cross-cutting fractures by relative timing, which is difficult to do¹¹. Absolute dating techniques (e.g. refs. 12,13), however, can assist in establishing the formation ages of individual fracture sets, thus permitting us to separate out a specific fracture event in absolute time. Assessing the secondary structural permeability associated with these fractures at the time of their formation remains, however, always challenging. Indeed, secondary permeability is both transient and dynamic, being first created by fracturing and then rapidly destroyed by the precipitation of different vein-infilling minerals within relatively brief spans of geological time^{10,14–16}. Even so, the opening and sealing of fractures can involve highly variable time scales between 10^3 and 10^6 years or more depending on a variety of factors such as fracture aperture, fluid chemistry and flow^{16–19}. Accordingly, evidence of paleo-permeability in

¹Department of Biological, Geological and Environmental Sciences, University of Bologna, Bologna, Italy. ²WSP UK Ltd., Edinburgh, United Kingdom. ³Geological Survey of Norway (NGU), Trondheim, Norway. e-mail: matthew.hodge@unibo.it; giulio.viola3@unibo.it

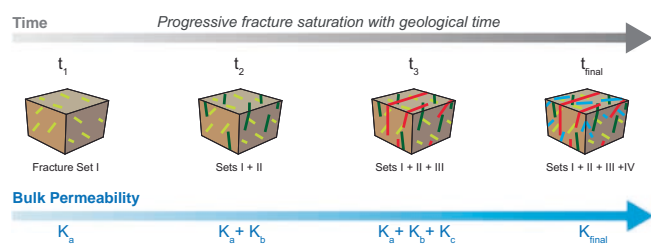


Fig. 1 | Conceptual framework of this study, highlighting the progressive saturation of the rock volume with fractures through time. Polyphase deformation leads to a progressive increase in fractures (coloured by set) through time (t). Corresponding to the sequential fracture formation events, bulk rock petrophysical properties, such as secondary permeability (K) cumulatively evolve with time. The final time stage (t_{final}) representing the sum of previous fracture events, and current fractured rock volume, also coincides with the present secondary permeability quality.

fractured media today can be represented by sealed to vuggy, propped, and open fractures depending on the scale and age of the features^{16,20,21}.

To address these challenges, we present a case study using a stochastic approach to reconstruct complex fracture networks in absolute time, replicating the transient permeability and fracture connectivity evolution of a selected rock volume. Fracture networks are routinely modelled using the discrete fracture network (DFN) approach (e.g. refs. 22–25), which relies on inputs such as fracture size, intensity, shape, orientation, and aperture²⁶ to generate statistically sound three-dimensional (3D) geometric fracture representations. These ‘static’ DFN models (representing the geometric description of one single geological moment) are then used to simulate a range of bulk rock petrophysical properties, such as permeability and fracture connectivity²⁵. To make our stochastic approach time-integrated, we implemented the ‘grown’ FracMan²⁷ DFN modelling method^{28–30}, whereby modelled fractures ‘grow’ in sequential time steps, with dynamic interactions between fractures²⁹. Crucially, this approach can replicate complex fracture networks involving multiple fracture sets of different relative ages, with younger fractures being affected by older pre-existing fractures²⁹.

As DFN modelling inputs we used a combination of multiscale deterministic datasets and temporal constraints provided by ref. 31 from Smøla island, mid-Norwegian passive margin (Fig. 2a). Smøla is an ideal setting for this study, it being a crystalline basement exposure that has experienced at least five deformation episodes from the Devonian to Early Palaeogene, which formed complex fracture and fault arrays that have been comprehensively structurally characterised and dated³¹. Using these inputs, we could therefore generate multiple DFN models representing distinct yet interacting fracture networks from the present day back to the Palaeozoic, quantifying the associated and progressive evolution of key petrophysical and network properties through geological time.

Our modelling shows that bulk permeability and fracture connectivity generally increased through geological time with progressive fracture saturation. To test the approach and validate our results, we used known events of hydrocarbon secondary migration and their timing offshore Norway. Our modelled events of enhanced permeability and connectivity values do coincide with the onset of most secondary migration activity in the Mid-Cretaceous, thus showing how past reservoir charging can be related to progressive secondary permeability enhancement in response to connectivity development. Furthermore, our determined maximum permeability orientations (as part of the permeability tensor anisotropy) highlight which fracture sets may have represented important fluid pathways at that time.

Results

Smøla island (Fig. 2a) is comprised of crystalline basement rocks (including monzogranite, diorite, gabbro)³¹, which typically have low matrix

permeability (between 10^{-18} and 10^{-19} m²)³². To generate our DFN models, we used numerous input parameters, which are described below, and in more detail in the Supplementary Information (Supplementary Methods 1 & 2). Crucial to enabling us to undertake this study, we have made use of multiscale spatial datasets (lineament trace mapping), high-resolution drill hole and field mapping datasets, and absolute dating of brittle deformation.

Deterministic inputs

Surface lineament traces on Smøla (Fig. 2) were mapped at four scales (deterministic trace maps: 1:500, 1:7 500, 1:25 000, and 1:100 000) on orthophoto imagery, digital terrain models (DTM), and aeromagnetic survey data. A total of 9554 fracture traces were picked and the distribution of their trace lengths over four orders of magnitude is best accounted for by a power-law relationship (Fig. 3). The power-law distributions, indicate that the number of fractures of relative lengths is consistent across multiple scales (exhibiting a fractal fracture pattern), let us model the fracture networks at our chosen volume dimensions. Lineament trace mapping provided the fracture size distributions and scaling exponents for each of the four identified lineament sets, which are oriented ~ N-S (to NNE-SSW), NE-SW, E-W, and NW-SE (to WNW-ESE). The details of these parameters are available in the Supplementary Methods 1.

In addition to the two-dimensional (2D) multiscale datasets, downhole televiwer data from four oriented diamond drill holes (by the Geological Survey of Norway-NGU) afforded crucial in-situ geometric information on drill-intersected structures (Fig. 4a). These data were sorted by pole to plane clusters, with twelve fracture sets identified over the four drill holes (Fig. 4a). Ref. 31 interpreted five deformation episodes (labelled D₁ to D₅) with associated systematic fracture sets on Smøla from field mapping and high-resolution logging of the same four oriented diamond drill holes. Each set is associated with distinct regional geometric trends, synkinematic mineralisations (Fig. 4b, c), different deformation episodes, deformation ages derived from K-Ar geochronology of fault gouges³¹ and U-Pb dating from other studies³³. Comparing both the downhole televiwer data to the field studies by ref. 31, the following five fracture sets from the televiwer data were thus selected for the DFN modelling (Tables 1, 2) and associated with drill hole linear fracture intensities (P_{10} , refer to Supplementary Methods 1), fracture characteristics (from fieldwork and drill logging), and ages:

- i) The earliest D₁ fractures (mean pole plunge and trend orientation: 01/123) are mostly tensile veins (locally associated with cataclastic bands), infilled by epidote-prehnite mineralisations (Fig. 4c) and have been associated with a post-Caledonian deformation episode >395 Ma based on a study from the Bergen area further to the SW of Smøla (Western Norway)³⁴;
- ii) The two D₂ fracture sets (mean pole plunge and trend orientation: 00/173 and 74.5/107) are shear features associated with sericite-chlorite-carbonate mineralisations (Fig. 4c), and were dated to ~300 Ma and ~204–196 Ma³¹;
- iii) D₃ fractures (mean pole plunge and trend orientation: 10/075) are shear fractures (with local breccias) decorated by chlorite-haematite mineral coatings (Fig. 4c) and were dated to ~128–100 Ma³¹;
- iv) The D₄ and D₅ fracture sets were grouped together for simplicity, owing to similar geometries (mean pole plunge and trend orientation: 08/242), and are both mostly tensile features, formed post ~75 Ma (70–60 Ma)^{31,33} with quartz-calcite-zeolite vein infill (Fig. 4c).

DFN modelling

Using the deterministic input values above, we applied the stochastic ‘grown’ DFN modelling approach described by refs. 29,30 to generate five fracture sets within a 500 m³ modelling volume. These fracture sets, which represent the natural fracture trends that accumulated in the Smøla basement during progressive deformation episodes, were used to model the D₁, D₂, D₃, and D₄ and D₅ (labelled as D₄₊₅) fracture sets.

From the drill hole televiwer data, each of the selected fracture sets has a statistical orientation distribution (Table 1), and an associated target

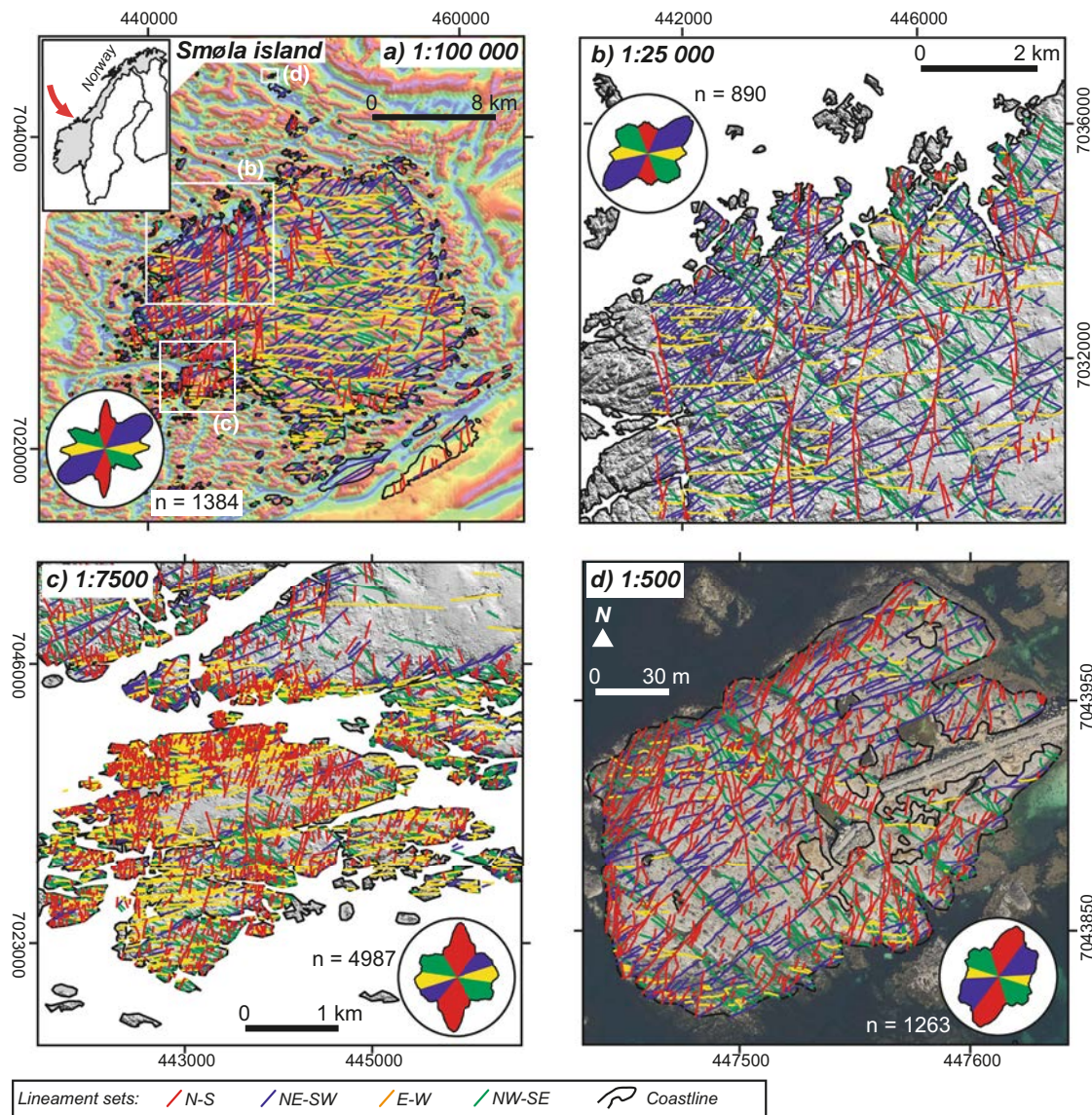


Fig. 2 | Trace maps over different portions of Smøla at different scales. Mapped lineament traces are coloured by azimuth trend (N-S coloured red, NE-SW coloured blue, E-W coloured yellow, and NW-SE coloured green), with associated rose plots showing the azimuth frequency trends. **a** shows the 1:100,000 trace map, **b** the 1:25,000 trace map, **c** the 1:7,500 trace map, and **d** the 1:500 trace map. Location of

Smøla island study area within the mid-Norwegian passive margin is shown in **(a)**. Locations of the **(b)** to **(d)** are shown with white boxes over Smøla island in **(a)**. All the base maps, including geophysical imagery, digital elevation data, and orthophoto imagery is courtesy of the NGU.

volumetric fracture intensity (P_{32}) converted from the relevant downhole linear fracture intensity (P_{10}) as shown on Table 2. Lower-limit P_{32} values were also calculated for comparison from the areal intensity (P_{21}) values from the 1:500 trace map lineaments (Fig. 2d; see Supplementary Methods 1). Each fracture set is attributed a related fracture size (minimum and cut-off size), and a power-law size exponent (α ; Fig. 3) from the lineament trace maps. Internal fracture properties are also provided for each set, such as aperture values (appraised from extensive drill core vein and fracture measurements, Supplementary Fig. 2) and fracture permeability. All the modelled fractures are assumed to not be sealed for this exercise. Termination relationships (Table 3) between the different lineament traces, which have been correlated to the fracture sets, were also included in the modelling. Further information is provided in Supplementary Methods 1 regarding all the input parameters.

Four ‘grown’ DFN models were stochastically generated as single realisations (Fig. 5), starting with the D_{4+5} model representing the current fractured rock volume on Smøla (post ~75 Ma). For each temporal iteration, fracture sets of younger sequential ages were progressively removed (back-

stripped). The first model (D_{4+5}) thus contains five fracture sets (8,244,732 individual fractures), with an average P_{32} value of 1.56 m^{-1} , and contains fractures formed during all the deformation episodes (D_1 to D_5). The second model, with four fracture sets (5,206,985 individual fractures) and an average P_{32} value of 1.3 m^{-1} , represents the rock volume post- D_3 deformation (~128–100 Ma). The third model, with three fracture sets (5,193,773 individual fractures), and an average P_{32} value of 1.24 m^{-1} , represents the volume after D_2 (~300 Ma and ~204–196 Ma). The fourth model, with one fracture set (10 107 858 individual fractures) and an average 0.67 m^{-1} P_{32} value, represents the volume post- D_1 deformation (>395 Ma).

Within the 500 m^3 modelling volumes, we nested a second 200 m^3 grid volume with 1000 grid cells (Fig. 5). The 200 m^3 grid was then used to estimate P_{32} volumetric intensities and, using the ‘Oda crack tensor’ from ref. 35, the equivalent permeability tensor for each grid cell³⁵. From the permeability tensor output (magnitude and orientation), the principal permeability axes (K_i), subdivided into maximum (K_1), intermediate (K_2), and minimum (K_3) eigenvectors, could be estimated. For each deformation episode, the three eigenvectors for each of the 1000 grid cells are plotted as

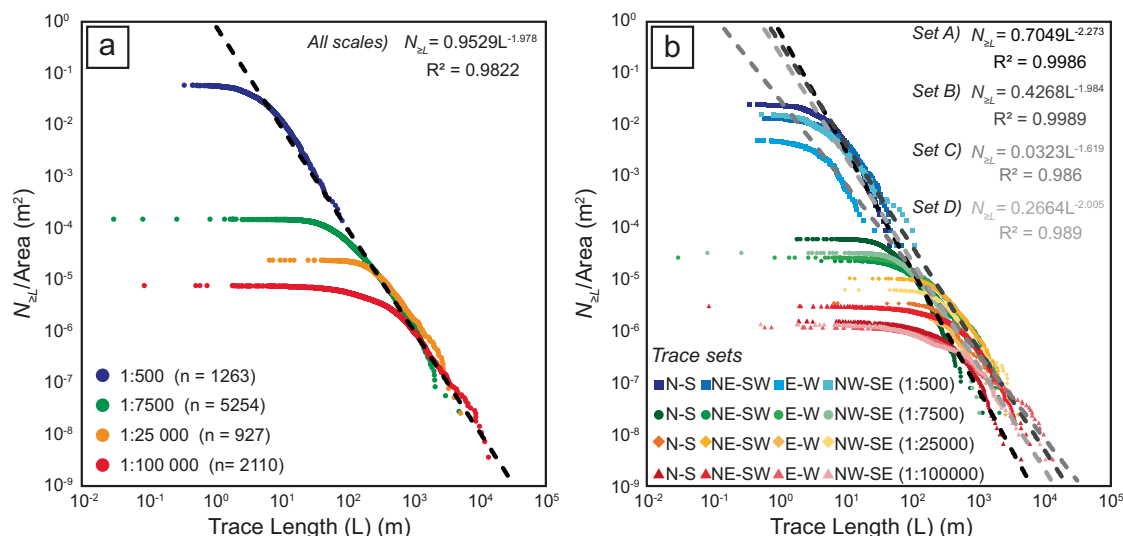


Fig. 3 | Cumulative fracture number vs. trace length log-log plots. **a** All the mapped lineament traces coloured by map scale; **b** mapped lineament traces subdivided and coloured by azimuth trend and mapped scale. For **(a)** and **(b)** the

associated linear regression lines are shown relative to each trace length distribution, with the regression equation and R^2 value.

poles on stereoplots (Fig. 5). An overall mean eigenvector for each of the K_1 , K_2 , and K_3 poles was then plotted, providing the average 3D orientation of the principal permeability tensor components (Fig. 5).

The principal permeability tensor for the D_{4+5} DFN model represents the current permeability anisotropy of the fractured Smøla rock volume; the components exhibit a sub-vertical K_1 , a sub-horizontal K_2 oriented NNW, and a K_3 oriented WSW. The average permeability values are $4.44e-13$ m² for K_1 , $4.01e-13$ m² for K_2 , and $1.77e-14$ m² for K_3 ($K_1 > K_2 > K_3$). The D_3 tensor components show a K_1 oriented sub-vertically, K_2 oriented ~S, and K_3 oriented ~W to WNW. The permeability values are ~1.6 orders of magnitude lower than those for D_{4+5} , with K_1 at $3.25e-13$ m², K_2 at $2.84e-13$ m², and K_3 at $1.31e-13$ m². The D_2 tensor has a sub-horizontal K_1 oriented ENE-WSW, a sub-vertical intermediate K_2 , and a K_3 oriented NNW-SSE. The average permeability values are ~1.7 orders of magnitude lower than D_3 , with $2.06e-13$ m² for K_1 , $1.55e-13$ m² for K_2 , and $1.10e-13$ m² for K_3 . For D_1 , the earliest permeability tensor, K_1 is sub-vertical to steeply inclined, K_2 is shallowly plunging to sub-horizontal and oriented NNE to NE, and K_3 is oriented NW. The average permeability values are ~2.2 orders of magnitude lower than D_2 , with K_1 at $9.47e-14$ m², K_2 at $9.36e-14$ m², and K_3 at $1.55e-14$ m² ($K_1 \approx K_2 > K_3$). Overall, there is a consistent increase in the principal permeability tensor magnitude through time periods from D_1 to D_{4+5} (increase of ~2.6 (for K_1), ~2.5 (for K_2), and ~3 orders of magnitude (for K_3)).

The principal permeability tensor component orientations and magnitudes are strongly influenced by the youngest fracture set(s) in each DFN model (most evident in the D_1 model). In the D_3 and D_{4+5} models the sub-vertical intersections between the different steeply dipping fracture sets result in K_1 orientations typically sub-vertical and parallel to these intersections. The D_2 model, however, is a combination of these two situations, with the sub-horizontal intersections of the two D_2 fracture sets and the earlier D_1 fracture set causing K_1 to be sub-horizontal. In general, the principal permeability eigenvector orientations rotate between the models, with K_2 (or K_1 for D_2) changing from towards the NE, to S, then NNW, and K_3 shifting from NW, NNW to W, WSW from D_2 to D_3 (Fig. 5).

Topology and fracture connectivity analysis

Both the 3D modelled fractures (Fig. 6a) and the 2D mapped (deterministic) lineament traces (Fig. 6b) have been quantitatively characterised, following the methodology of ref. 36, for network topology and spatial connectivity (Fig. 6c). To make comparisons with the final DFN (D_{4+5}) model (representing the same time interval as the deterministic trace maps), and to

confirm scale-independent self-similarity between the different deterministic trace maps (mapped at various scales from different parts of Smøla; Fig. 2 & Supplementary Fig. 1), all the trace maps were analysed using a branch and node counting method³⁷. The proportional counts of branches and nodes were then used to confirm whether the maps form part of the same fracture system and to obtain network topology and connectivity characteristics.

Four modelled trace maps were produced with the 3D fractures represented as 2D lines on horizontal slices through each of the four DFN models (traces being intersection lineations on the planar surface). Three circular representative scan areas (20 m diameters) were selected within each model trace map for network topology analysis (selected scan areas shown on Fig. 6a). The branch types include I-I (isolated), C-I (semi-isolated), and C-C (connected)-type branches. The nodes counted included I (isolated), Y (terminating), and X (cross-cutting), and E (edge)-type nodes³⁶. In total, 2001 nodes and 2530 branches were counted across the maps. Subsequently, each of the four deterministic lineament trace maps was similarly analysed following the same procedure. For each trace map at the different scales, we selected three circular representative scan areas from 4 m (1:100 000) to 40 m (1:500) in diameter. Within each scan area, all the network branches and nodes were similarly counted (selected scan areas shown on Fig. 6b). Overall, 2685 branches and 2154 nodes were counted for all the different scales. Further information is available in the Supplementary Methods 2.

The topology ternary diagrams of Fig. 6c plot the proportions of nodes and branches from the modelled and deterministic trace maps. Out of the modelled trace maps, the D_1 trace map yielded the highest proportion of I-nodes (~76 %), with D_2 and D_3 having the highest number of X-nodes (~41% and ~45 % respectively), and D_{4+5} the highest proportion of Y-nodes (~32 %). In contrast, the deterministic trace maps show on the node ternary plot that the 1:500 trace map has the highest proportion of Y-nodes (~64 %), while the 1:7500 and the 1:100,000 trace maps exhibit the highest proportion of I-nodes (~41 % and 38 %, respectively). Overall, X-nodes become more abundant with the increasing scale (~9 % to 24 %), suggesting that the resolution of lineament mapping may affect the detection of node type. For all the maps, however, X-nodes are less common than other node types. The final modelled D_{4+5} trace map has fewer Y-nodes, but a similar abundance of C-C branches as the mapped lineament trace maps across the scales. Overall, the modelled trace maps back through time show a trend of increasing number of isolated branches and nodes. Finally, the similar branch and node proportions in the deterministic trace maps suggest they

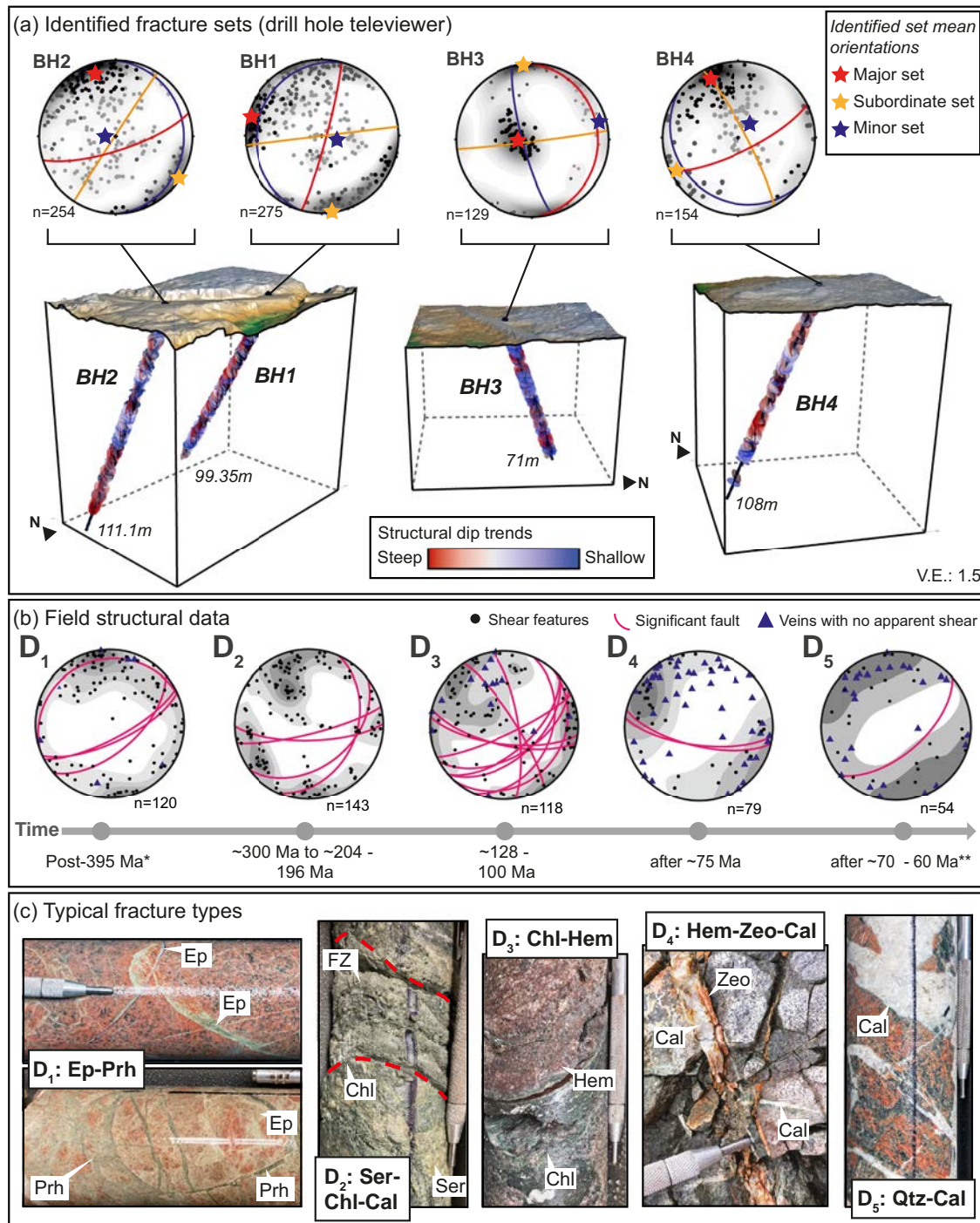


Fig. 4 | Drill hole structural data and field data utilised in the study. **a** 3D blocks of the four drill holes used in the study with downhole televiewer structural data coloured by dip to demonstrate geometric trends. The televiewer data shown in the stereonets are sorted by fracture sets. All the stereonets are Equal Area, lower hemisphere projected, Kamb contoured at the 2σ interval, and Terzaghi corrected based on the azimuth and inclination of the drill hole surveys (maximum correlation

factor of 7), V.E = vertical exaggeration (also refer to Supplementary Table 2). **b** Field data sorted by deformation episode based on mineral assemblage and relative or absolute age or timing and modified from ref. 31. Absolute ages provided by *ref. 33, and **ref. 34. **c** Typical fracture types as seen in drill core and field outcrops. Mineral types are Ep = epidote, Prh = prehnite, Chl = chlorite, Ser = sericite, Hem = haematite, Cal = calcite, Zeo = zeolite, Qtz = quartz.

belong to the same fracture system, supporting the use of lineament trace-derived fracture length distributions (Fig. 3) in our DFN modelling.

To assess fracture connectivity for the modelled and deterministic maps (Fig. 6c), we used the ‘connections per branch’ (C_B) average value (combined for each scale’s scan areas). The C_B parameter is defined as $C_B = (3N_Y + 4N_X) / N_B$, where N_Y is the number of Y-nodes, N_X is the number of X-nodes, and N_B is the total number of branches expressed as $0.0 < C_B < 2.0$ ³⁶. In this example, rather than using the ‘effective’

connectivity, which would have to take fracture sealing into account, we use the ‘apparent’ connectivity that accounts for all present fractures (and related branches and nodes) irrespective of the openness (e.g. ref. 38). For the modelled trace maps, the calculated C_B values are 1.01 for D₁, 1.74 for D₂, 1.82 for D₃, and 1.79 for D₄₊₅. In time, the networks become therefore well-connected from D₂ onwards, indicating an evolution in the interconnectivity of the fracture system through time following a general trend towards higher connectivity with progressive fracture saturation. For

comparison, the deterministic lineament traces have calculated C_B values of 1.5 for the 1:100 000 map, 1.75 for 1:25 000, 1.65 for 1:7 500, and 1.8 for the 1:500 map. In general, all the maps have C_B values > 1.5, suggesting a good degree of interconnectivity on average. Importantly, the C_B values, and the proportions of branches and nodes for the D_{4+5} modelled trace maps, overlap well and show similarity to the lower-resolution deterministic trace maps (1:100 000 and 1:25 000).

Discussion

The variety of our deterministic inputs and our stochastic approach allowed us to estimate the evolution of secondary permeability and fracture connectivity within a fractured basement rock volume over geological time. The petrophysical conditions allocated to the recognised, characterised, and dated deformation episodes are assumed to have existed at distinct times corresponding to our D_1 to D_{4+5} models and have evolved with time.

Fractures forming by brittle failure may result from transient fault-valve behaviour, controlled by critical combinations of pore-fluid pressure and differential stress conditions^{14,15}. Assuming this, fractures can form and progressively evolve during each deformation episode, as also shown by crack-and-seal vein textures in some of the veins on Smøla³¹. During the episodes, dynamic conditions existed where paleo-apertures, represented by transiently open fractures, repeatedly formed allowing fluid ingress and flow¹⁵. These open fractures were also repeatedly sealed in brief geological time spans by the precipitation of vein minerals³⁹. Maximum caution is thus necessary when discussing bulk petrophysical characteristics, as they represent not only the effects of transient conditions but may also be the result of multiple events during a single deformation episode that we are now grouping together. Furthermore, as fracture sealing will decrease connectivity through time², our modelling only considers the apparent connectivity related to assumed open fractures and not necessarily connectivity related to active fluid flow pathways.

Evolution in secondary permeability and fracture connectivity through time

Remarkably our modelling results make it possible to assess how permeability anisotropy and fracture connectivity have varied through time during

the evolution of a tract of the mid-Norwegian passive margin. Insights into how the actual geology of Smøla impacted the results are discussed below. For ease of comparison between the different DFN models, we project our computed maximum and intermediate permeability eigenvectors (K_1 and K_2) of the 3D permeability tensor components onto the 2D horizontal plane as the estimated maximum permeability direction (K_{Hmax} ; Fig. 7).

Model D_{4+5} (Fig. 5) represents the current fractured rock volume, which is the sum of the accumulated fractures from the Devonian to at least the Late-Cretaceous-Palaeogene (<75–60 Ma). The model predicts a bulk NNW-SSE oriented K_{Hmax} (Fig. 7), which reflects all the earlier and newly formed fractures. Compared to the earlier models (D_1 to D_3), this model has the highest principal permeability tensor (PPT) component magnitudes ($4.44e-13\text{ m}^2$ for K_1 to $1.77e-14\text{ m}^2$ for K_3), implying that PPT magnitude increases with fracture saturation related to increasing numbers of (inter-connected) fracture sets. During late-Cretaceous to Tertiary times, fluid migration would have therefore focussed along structures oriented ~NNW-SSE (sub-parallel to our K_{Hmax}) with steep dips (K_1 sub-vertical), before later mineral precipitation (calcite-quartz-zeolite in our case³¹) and infill (e.g. ref. 14). Despite the relative high permeability, the D_{4+5} model has lower connectivity ($C_B = 1.79$) compared to the earlier D_3 model ($C_B = 1.82$) (Fig. 7). Influencing the C_B modelled connectivity, the D_{4+5} veins are commonly isolated features, rarely cross-cutting older features (contributing few X-nodes), and commonly utilise pre-existing fractures (reactivating older fractures as tensile veins³¹), which would indeed result in lower fracture connectivity. But, as fracture sealing is not incorporated in our modelling, the effective connectivity should not decrease (as isolated branches will only affect the apparent connectivity measure, not effective connectivity), as it can only increase or remain constant during the addition of new fracture sets.

Back-stripping out the D_{4+5} fractures, model D_3 represents the rock volume during the mid-Cretaceous (~128–100 Ma). It constrains a N-S to NNW-SSE K_{Hmax} (Fig. 7), and lower PPT magnitudes ($3.25e-13\text{ m}^2$ for K_1 to $1.31e-13\text{ m}^2$ for K_3). Potential fluid flow during the mid-Cretaceous would thus have occurred along fractures oriented sub-parallel to this K_{Hmax} orientation. In terms of connectivity, the fracture termination relationships (Table 3) promoted abundant cross-cutting traces for the D_3 model, which, in turn, resulted in the highest obtained fracture connectivity ($C_B = 1.82$; Fig. 7). The fracture orientation trends used here shift dramatically from D_2 to D_3 (~E-W to N-S; Fig. 5), which correlates with a regional stress-field shift in mid-Norway in the mid-Cretaceous⁴⁰. Whether this is the cause for new cross-cutting fractures rather than reactivating earlier D_2 or D_1 fractures is not however clear. Notably, though, the D_3 fractures are indurated and infilled with cataclastic (to gouge; chlorite-haematite mineralised)³¹. Possible fluid ingress into these fractures may have been thus aided by host rock clasts potentially ‘propping’ the features open during fluid flow events⁴¹. Overall, the D_3 model supports major fluid flow during the mid-Cretaceous, with relatively high permeability magnitudes (aided by ‘propped’ fractures), and the highest fracture connectivity.

After stripping out the D_3 fracture set, the D_2 model reproduces the rock volume during the Late Carboniferous to Permian and the late Triassic to early Jurassic (~300 Ma to ~204–196 Ma). For that time, modelling

Table 1 | Mean orientations of selected fracture sets from the downhole televiewer data

Drill Hole	Fracture Set	Fracture Count	Mean Pole Trend (°)	Mean Pole Plunge (°)	Def. Episode
BH2	NE-SW	53	122.9	0.66	D_1
BH1	E-W	122	173.2	0.19	D_2
BH1	Shallow	133	106.7	74.53	D_2
BH3	N-S	31	74.65	10.04	D_3
BH4	NW-SE	31	242.04	8.02	D_{4+5}

Fracture sets are classified by general strike orientation, except for the ‘Shallow’ set, which represents the shallowly dipping D_2 fracture set.

Table 2 | Key model input parameters by fracture sets and ordered by deformation episode

Fracture Set Name	P_{10} (1 m^{-1})	P_{32}^* ($\text{m}^2\cdot\text{m}^{-3}$)	Target P_{32} used				Size (min) (m)	Size (max) (m)	Scaling exponent (α)	Aperture (mm)	K (m^2)
			D_1	D_2	D_3	D_{4+5}					
NE-SW	0.48	0.76	0.6	0.3	0.3	0.3	1	20	1.984	0.03	$5.1e-12$
E-W	1.07	1.68		0.5	0.3	0.3	10	80	1.619	0.04	$5.1e-12$
Shallow	1.17	1.84		0.4	0.2	0.2	5	60	1.619	0.04	$5.1e-12$
N-S	0.44	0.66			0.6	0.3	10	80	2.273	0.09	$5.1e-12$
NW-SE	0.29	0.47				0.5	5	45	2.005	0.1	$5.1e-12$

The fracture intensity P_{32} values are estimated from P_{10} using the *ref. 63 conversion method. Refer to the Supplementary Methods 1 for further information on the target P_{32} values used. Truncation sizes (min = minimum, max = maximum) relate to equivalent radius of modelled fractures. K stands for permeability value of the fracture infill.

yielded a permeability anisotropy K_{Hmax} oriented NE-SW to ENE-WSW, with a sub-horizontal K_1 orientation (K_1 is sub-vertical in the other models), with the second-lowest PPT magnitudes ($2.06e-13 m^2$ for K_1 to $1.10e-13 m^2$ for K_3). The D_2 model represents a prolonged episode, which we modelled by means of three fracture sets (two for D_2 and one for D_1). Both D_2 sets contain phyllosilicate-rich (chlorite-sericite) phyllite shears to shear fractures, with fault gouge³¹. In fact, the D_2 fractures type and the orientation of the permeability anisotropy indicate complex fluid-flow regimes along

either the sub-vertical ~E-W structures or laterally along shallowly dipping structures (as suggested by the K_1 orientation). Further complicating this picture, authigenic phyllosilicates may have impeded potential fluid flow (which our modelling ignores), with the D_2 fractures later acting as impermeable barriers⁴². Irrespectively, the fracture connectivity of this model, being nearly equal to the D_3 and D_{4+5} models, does demonstrate how a high degree of connectivity ($C_B > 1.5$) was achieved by the late Triassic. The sudden increase in C_B indicates that, at this resolution, fracture networks rapidly become interconnected during deformation (e.g. ref. 10).

Finally, back-stripping out the D_2 fracture set, only the earliest initial fractures remain, recreating the basement volume during the Devonian (>395 Ma). The D_1 model, with early tensile epidote-prehnite veins³¹ infilling those fractures, provides a NE-SW oriented K_{Hmax} and the lowest PPT magnitudes ($9.47e-14 m^2$ for K_1 to $1.55e-14 m^2$ for K_3) (Fig. 7), ~3 orders of magnitude lower than the D_{4+5} model. Overall, the D_1 model reflects the mostly isolated modelled fractures and is the least connected of all DFN models, with a C_B value of 1.01. The low C_B value notwithstanding, owing to the low permeability of the host rock, these initial fractures may still have imparted an important bulk permeability anisotropy, with fluid flow during the Devonian focused along hydraulically connected fractures sub-parallel to the K_{Hmax} where available.

Table 3 | Probability of termination (%) of a younger mapped lineament trace set against an older ‘passive’ set

		Younger (lineament trace sets)			
		NE-SW	E-W	N-S	NW-SE
Older	NE-SW	19%	21%	15%	27%
	E-W	39%	36%	67%	31%
	N-S	16%	27%	6%	30%
	NW-SE	26%	16%	12%	12%

Based on geometric similarity to the fracture sets (Table 1), the NE-SW traces are associated with D_1 , the E-W traces with D_2 , the N-S traces with D_3 , and the NW-SE traces with D_{4+5} for the modelling. The ‘Shallow’ fracture set has no corresponding lineament set, as there is no clear 2D map view trace. The adjusted termination probability values used (including for the ‘Shallow’ set), are detailed in the Supplementary Methods 1.

Reactivation

As the host rock matrix permeability is intrinsically very low, the fracture sets modelled are the basement’s most permeable features. However,

Fig. 5 | DFN model outputs with fractures back-stripped out of each deformation episode (D_{4+5} to D_1) through geological time. For each $500 m^3$ DFN model, the fracture upscaling grid outputs ($200 m^3$) are shown below with the 1000 grid cells coloured by maximum permeability eigenvector (K_1) value (m^2); the principal permeability tensor (PPT) axes K_1 (red star), K_2 (green box), K_3 (blue circle) are indicated in terms of orientation (on stereonet plots) and relative magnitude (m^2) (box plots) for each deformation episode. Illustrative box plots display the inter-quartile region (boxes; 50 % of permeability magnitudes), and whiskers which extend to the first and third quartiles, respectively. Mean permeability magnitude values are not shown.

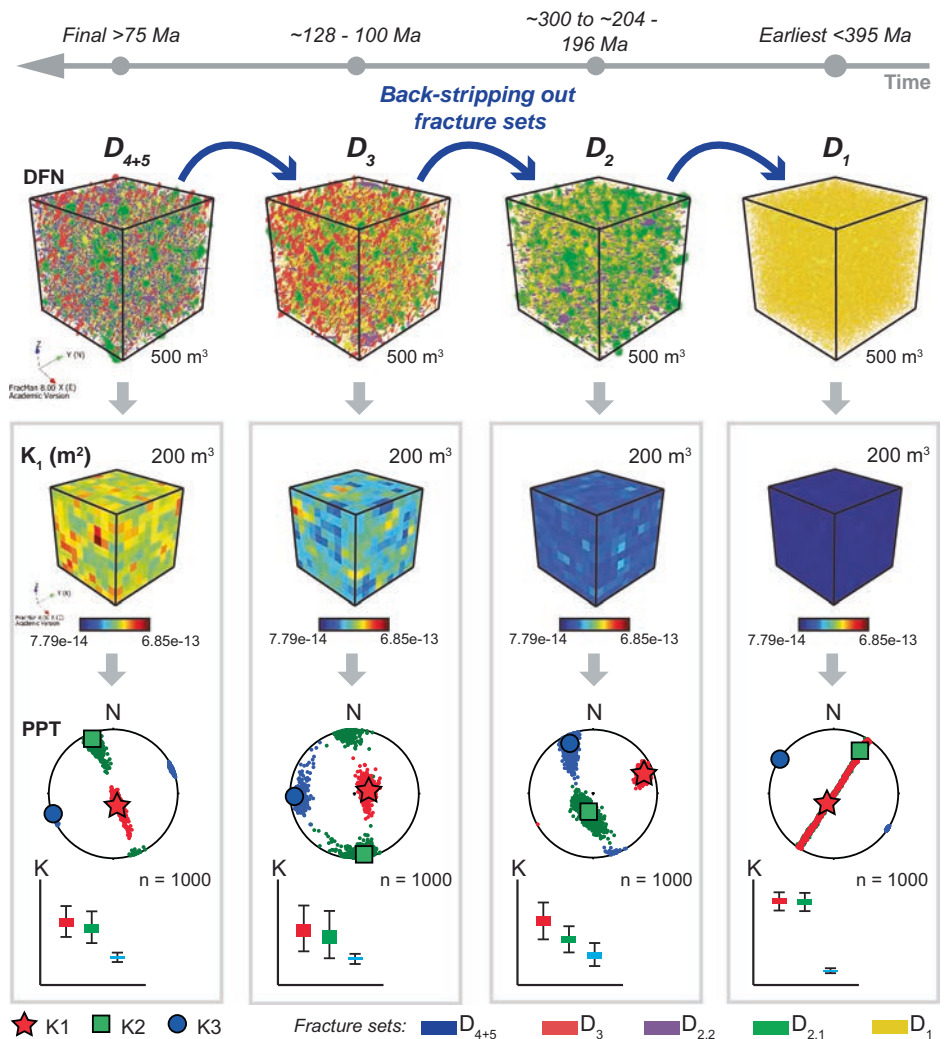
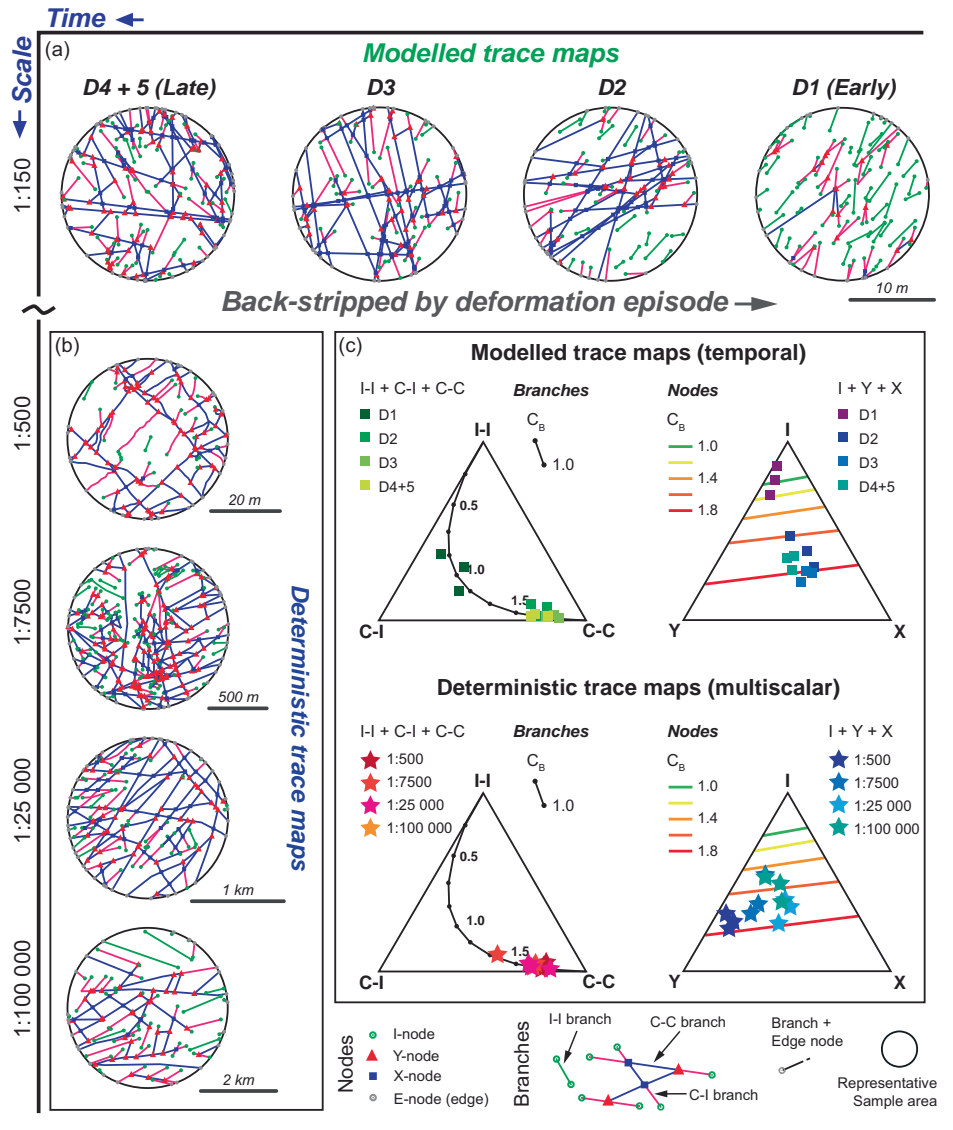


Fig. 6 | Network topology analysis results.

a Representative 2D trace maps, extracted from the 500 m³ DFN models, shown back-stripped through time, and **b** multiscalar deterministic trace maps for comparison (all representing the same deformation episode as the D₄₊₅ model trace map, with all deterministic trace maps shown on Supplementary Fig. 3. **c** Ternary plots illustrating the proportions of both nodes and branches for both modelled (single realisation) trace maps, with data points (blocks) coloured by deformation episode; and deterministic trace maps (representative scan areas), with the data points (stars) coloured by scan area scale.



without clear control on the reactivation of pre-existing features, it is challenging to fully constrain the 3D principal permeability tensor. Our modelling addresses this by incorporating pre-existing features with lower volumetric intensity, P_{32} values (typically decreased by ~50 % from their initial intensity value) to try and simulate selective reactivation. A noteworthy limitation in our modelling, however, concerns fracture reactivation between different DFN model generations.

Assuming adequate pore fluid pressures, and necessary cohesion and shear strength values^{43,44}, fractures optimally oriented 30° to the maximum principal stress (σ_1) and containing the intermediate principal stress (σ_2) should reactivate as shear fractures, while those oriented ~0° to σ_1 (and containing σ_2) should reactivate as tensile fractures (with fractures between these two endmember situations reactivating as hybrid fractures)^{44,45}.

For Smøla, the stress fields during the Triassic-Jurassic (D₂) and Early to Late Cretaceous (D₃ and potentially D₄₊₅) indicate a least compressive stress (σ_3) oriented E-W and NW-SE to WNW-ESE, respectively⁴⁰. The stress field orientations suggest that, assuming a sub-vertical σ_1 (maximum horizontal stress $\approx \sigma_2$), a portion of favourably oriented fractures from D₁ to D₃ would have been progressively reactivated. Examples of this are late D₄₊₅ quartz-calcite tensile veins in both D₂ and D₃ fractures³¹. Considering mid-Norway's more recent glacial history, isostatic uplift from ice unloading may have also reactivated many low-angle fractures (sub-vertical σ_3)⁴⁶.

Quantifying the proportion of reactivating fractures in each DFN model remains unresolved. Dilation and shear tendency studies using

assumed paleostress fields may define statistical probabilities of reactivation, providing a basis for intensity estimates, and confirming bulk permeability trends, but this remains presently unanswered in this study.

Approach advantage and wider implications

Unique insights are offered by our approach, using selective back-stripping of components, formed at specific geological times, to study the evolution of selected petrophysical characteristics in crystalline basement blocks. A similar approach has previously been proposed only in a 3D tomography study of paleo-porosity evolution (e.g. ref. 47), and, in an opposite sense, in stepwise forward modelling (restoration) to understand progressive deformation and evolution of permeability (e.g. ref. 48). However, those studies lack absolute time constraints, making it difficult to place any results within geologically meaningful time frames. Other fracture network studies have demonstrated the evolution of fracture pattern development within absolute time frames (e.g. refs. 3,4,16). Those studies, however, typically have attributed fractures (and associated petrophysical properties) to formation ages through indirect means (for example, via thermal and burial ages, quartz accumulation rates, and dated paleostress-field trajectories). In contrast, our modelling benefits remarkably from an absolute time dimension and an unprecedented well-resolved structural characterisation of the fracture sets on Smøla. These constraints enabled us to precisely control the structure and timing of fracture formation in our DFN reconstructions. Additionally, the 'grown' DFN modelling approach includes

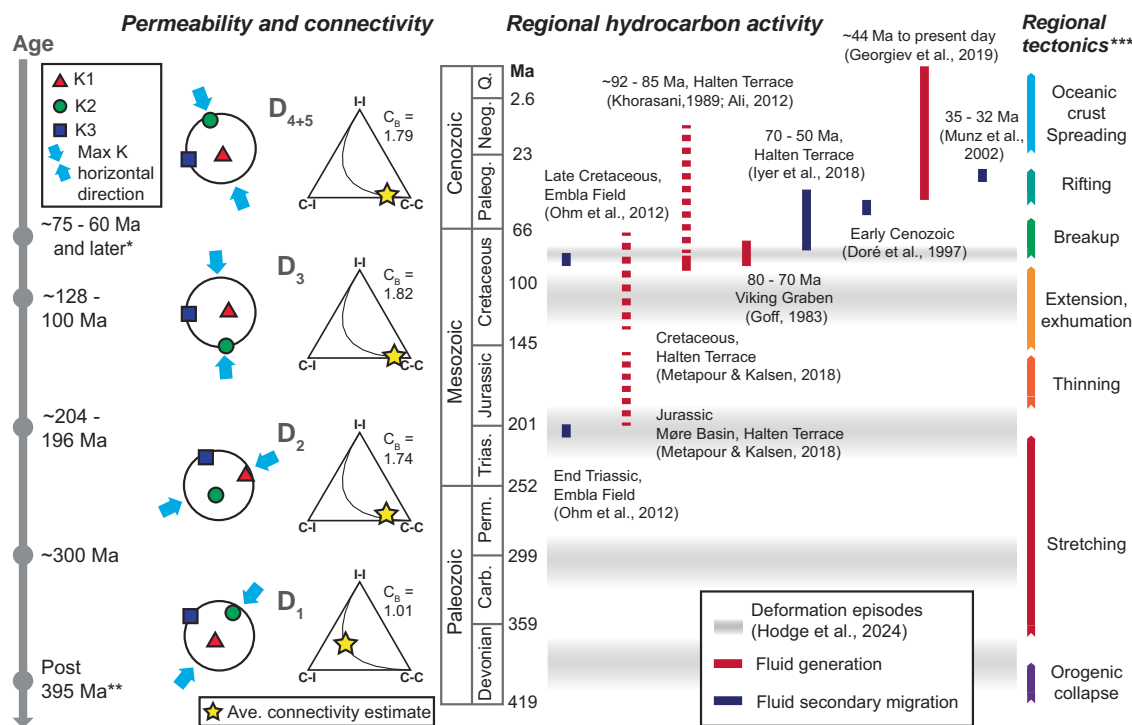


Fig. 7 | Comparison of the DFN modelling results relative to regional hydrocarbon and tectonic activity in geological time. The absolute time-constrained permeability anisotropy (simplified stereonet, with blue arrows indicating K_{Hmax} orientation) and fracture connectivity (ternary plots with yellow stars showing the

proportion of branch types) are shown relative to dated regional hydrocarbon generation (red bars), secondary migration (blue bars), and tectonic activity (coloured by tectonic stage). Ages provided by * ref. 33, and ** ref. 34, and tectonic stages modified *** from ref. 57.

temporal aspects related to fracture propagation and interaction^{29,49,50}, simulating pre-existing fractures, during each generation of DFN. Also, considering that sub-seismic-resolution faults and fractures (<10–30 m in size) in impermeable reservoirs may considerably affect fluid flow⁵¹, using the presented stochastic approach our modelling can model fractures at that resolution. The flexibility in modelling resolution is an advantage when comparing to 3D tomography (fine resolution on the mm to cm scale) and forward modelling techniques (large resolutions on the km scale).

To further test and validate our approach, we use hydrocarbon dynamics from offshore Norway as a useful example owing to available absolute time constraints. Hydrocarbons are generally dated using geochronology and biostratigraphic techniques such as Re-Os radiometric dating and biomarkers^{52,53}. Our DFN models with the associated ages can, therefore, be compared against known reservoir migration events (assuming our 500 m³ modelling volume and the 200 m³ fracture upscaling volume represent a typical reservoir, see Supplementary Methods 2 for further details), and broader tectonic events through geological time.

The D₂ DFN model, for example, temporally coincides with the earliest known episode of hydrocarbon generation and secondary migration (Triassic–Jurassic) in the Embla field (Late Triassic fluid migration) and the Halten Terrace (Jurassic oil generation)^{54,55} (Fig. 7). Even though hydrocarbon generation is linked to the burial and thermal history (maturation) of source rocks⁵⁶, subsequent tectonic activity may have led to enhanced fracturing and increased secondary permeability in adjacent rock volumes, potentially facilitating the secondary migration activity. The Triassic and Jurassic witnessed crustal stretching and thinning due to the rifting of Norway and Greenland⁵⁷ and strike-slip faulting along the Møre-Trøndelag Fault Complex (MTFC), a major NE–SW feature extending from Central Norway into the northern North Sea^{31,58}. Transtensional kinematics on the MTFC, splay development, and related extension influenced the orientation of the fracture sets that we have used for our modelling, with many being oblique to the strike of the MTFC. Despite hydrocarbon generation in the Halten Terrace during the Late Triassic to Jurassic, major reservoir-scale

secondary migration may have been limited owing to the lack of permeable or communicable E–W faults and reactivated NE–SW fractures.

During the Cretaceous to Paleogene (D₄₊₅ and D₃ models), most hydrocarbon generation and secondary migration events initiated, extending into the Neogene and later^{54,59–62} (Fig. 7). Remarkably, our D₃ and D₄₊₅ models temporally correspond to secondary migration events in the Halten Terrace (mid-Norwegian margin) and Viking Graben (SW Norway), such that we can tentatively suggest a link between secondary migration, reservoir charging, and fracturing as per our DFN modelling also at that time. However, assuming this migration activity is recorded by our modelling results, from the Cretaceous onwards, crustal extension of the newly forming passive margin led to major rift basins, basement structural highs (representing ‘buried hill-type’ hydrocarbon traps⁴¹) and NE–SW to NW–SE striking extensional faults, such as the Klakk fault complex oriented ~NNW–SSE (similar geometries as our D₃ and D₄₊₅ fracture sets). Therefore, structures oriented ~N–S to NW–SE forming during the Norway–Greenland rifting and break-up, being parallel to our K_{Hmax} orientations at these times, may well have been important fluid pathways during the Mid-Cretaceous (D₃) onwards. These conduits would enable communication between basin source rocks and potential trap sites, facilitating fluid percolation and reservoir charging of, for example, fractured basement plays with similar lithologies as Smøla.

As demonstrated by this example, our approach can be adapted to quantify similar geofluid migration histories and is applicable in various contexts where understanding the evolution of bulk rock permeability or fracture interconnectivity is crucial, such as in fracture-hosted groundwater systems, nuclear waste repositories, and CO₂ storage studies.

Conclusions

Our study offers a conceptual approach to constrain fracture-related petrophysical properties through time. Using temporally constrained basement-hosted fractures from Smøla, mid-Norwegian passive margin, stochastic modelling reconstructs the evolution of fractured rock volumes as

'grown' DFN models, from the present back to the Devonian. To improve realism, we integrated various deterministic remote sensing, geophysical, drill core, and field studies datasets, combined with absolute dating results, to generate stochastic DFN models with petrophysical estimates.

Our well-constrained orientation trends and sorting criteria of different fracture sets, along with absolute ages, allowed us to recreate the fractured rock volume during each deformation episode. By applying a back-stripping methodology to the fracture sets, we deconvoluted a complex present-day fracture network into four time-specific models representing the Late Cretaceous-Palaeocene (and later), the mid-Cretaceous, Late Triassic-Jurassic to Carboniferous-Permian, and finally the Devonian (spanning over ~300 Ma). Each of these models are stochastic representation of fracture networks back through time and provides estimates of the bulk principal permeability tensor (component orientations and magnitudes), and fracture connectivity at specific episodes in geological time.

Comparison of our results with an example of absolute-dated geofluid activity, namely petroleum secondary migration offshore Norway, shows that our modelled time-specific petrophysical characteristics fit well with known episodes of hydrocarbon activity and reservoir charging. The ability to estimate permeability and connectivity properties during past fluid migration events represents an important advancement in understanding fluid flow histories. Understanding how the orientation of permeability anisotropy has changed through geological time can indicate which structures were subparallel to the maximum permeability anisotropy and thus served as preferential fluid pathways during specific episodes. Additionally, identifying when peak fracture connectivity occurred, which in our example of offshore hydrocarbon activity was during the mid-Cretaceous, provides a basis for understanding why geofluid activity may have commenced at that time (notwithstanding the burial history and source rock maturation in our example).

While incorporating more geological characteristics that affect permeability (such as fracture infill types) and structural reactivation into our models remains beyond the scope of this study, those inputs could further refine similar approaches in the future. Nonetheless, the framework highlighted in this study remains statistically sound and can be adapted and applied broadly to other geological terranes where absolute time constraints on fractures are available, providing a novel perspective on the history of fluid flow in fractured media.

Data availability

The drill hole structural measurements (viewer log), paleo-aperture measurements, fracture trace map GIS shapefiles (modelled and deterministic), network topology data, and DFN output permeability tensor data utilised within this study, can be accessed online within the Mendeley Data repository (<https://data.mendeley.com/datasets/ctpphnptc5/2>) with the identifier <https://doi.org/10.17632/ctpphnptc5.2>.

Received: 21 August 2024; Accepted: 19 February 2025;

Published online: 05 March 2025

References

1. Olson, J. E., Laubach, S. E. & Lander, R. H. Combining diagenesis and mechanics to quantify fracture aperture distributions and fracture pattern permeability. *Geol. Soc. Lond. Spec. Publ.* **270**, 101–116 (2007).
2. Olson, J. E., Laubach, S. E. & Lander, R. H. Natural fracture characterization in tight gas sandstones: Integrating mechanics and diagenesis. *Am. Assoc. Pet. Geol. Bull.* **93**, 1535–1549 (2009).
3. Laubach, S. E. & Kira, D. T. Laurentian palaeostress trajectories and ephemeral fracture permeability, Cambrian Eriboll Formation sandstones west of the Moine Thrust Zone, NW Scotland. *J. Geol. Soc. Lond.* **166**, 349–362 (2009).
4. Engelder, T. & Geiser, P. On the use of regional joint sets as trajectories of paleostress fields during the development of the Appalachian Plateau, New York. *J. Geophys. Res. Solid Earth* **85**, 6319–6341 (1980).
5. Viola, G., Venvik Ganerød, G. & Wahlgren, C. H. Unraveling 1.5 Ga of brittle deformation history in the Laxemar-Simpevarp area, southeast Sweden: a contribution to the Swedish site investigation study for the disposal of highly radioactive nuclear waste. *Tectonics*. **28** <https://doi.org/10.1029/2009TC002461> (2009).
6. Drake, H., Tullborg, E. L. & Page, L. Distinguished multiple events of fracture mineralisation related to far-field orogenic effects in Paleoproterozoic crystalline rocks, Simpevarp area, SE Sweden. *Lithos* **110**, 37–49 (2009).
7. Viola, G., Kounov, A., Andreoli, M. A. G. & Mattila, J. Brittle tectonic evolution along the western margin of South Africa: More than 500Myr of continued reactivation. *Tectonophysics* **514–517**, 93–114 (2012).
8. Munier, R. & Talbot, C. J. Segmentation, fragmentation and jostling of cratonic basement in and near Äspö, southeast Sweden. *Tectonics* **12**, 713–727 (1993).
9. Mattila, J. & Viola, G. New constraints on 1.7 Gyr of brittle tectonic evolution in southwestern Finland derived from a structural study at the site of a potential nuclear waste repository (Olkiluoto Island). *J. Struct. Geol.* **67**, 50–74 (2014).
10. Cox, S. F. Coupling between Deformation, Fluid Pressures, and Fluid Flow in Ore-Producing Hydrothermal Systems at Depth in the Crust. In: *One Hundredth Anniversary Volume. Soc. Econ. Geol.* **39** <https://doi.org/10.5382/AV100.04> (2005).
11. Scheiber, T. & Viola, G. Complex bedrock fracture patterns: a multipronged approach to resolve their evolution in space and time. *Tectonics* **37**, 1030–1062 (2018).
12. Viola, G. et al. Deconvoluting complex structural histories archived in brittle fault zones. *Nat. Commun.* **7**, 13448 (2016).
13. Torgersen, E., Viola, G., Zwingmann, H. & Harris, C. Erratum to “Structural and temporal evolution of a reactivated brittle-ductile fault - Part II: Timing of fault initiation and reactivation by K-Ar dating of synkinematic illite/muscovite”. *Earth Planet. Sci. Lett.* **410**, 211 (2015).
14. Sibson, R. Crustal stress, faulting and fluid flow. *Geol. Soc. Lond. Spec. Publ.* **78**, 69–84 (1994).
15. Cox, S. F. The application of failure mode diagrams for exploring the roles of fluid pressure and stress states in controlling styles of fracture-controlled permeability enhancement in faults and shear zones. *Geofluids* **10**, 217–233 (2010).
16. Becker, S. P. et al. A 48 m.y. history of fracture opening, temperature, and fluid pressure: cretaceous Travis Peak Formation, East Texas basin. *GSA Bull.* **122**, 1081–1093 (2010).
17. Fisher, D. M. & Brantley, S. L. Models of quartz overgrowth and vein formation: Deformation and episodic fluid flow in an ancient subduction zone. *J. Geophys. Res. Solid Earth* **97**, 20043–20061 (1992).
18. Williams, R. T. & Fagereng, Å. The role of quartz cementation in the seismic cycle: a critical review. *Rev. Geophys.* **60**, e2021RG000768 (2022).
19. Lee, Y. J. & Morse, J. W. Calcite precipitation in synthetic veins: implications for the time and fluid volume necessary for vein filling. *Chem. Geol.* **156**, 151–170 (1999).
20. Hosono, H., Takemura, T., Asahina, D. & Otsubo, M. Estimation of paleo-permeability around a seismogenic fault based on permeability tensor from observable geometric information of quartz veins. *Earth Planets Space* **74**, 141 (2022).
21. Forstner, S. R. & Laubach, S. E. Scale-dependent fracture networks. *J. Struct. Geol.* **165**, 104748 (2022).
22. Long, J. C. S., Gilmour, P. & Witherspoon, P. A. A model for steady fluid flow in random three-dimensional networks of disc-shaped fractures. *Water Resour. Res.* **21**, 1105–1115 (1985).
23. Dershowitz, W. S. *Rock Joint Systems*. Doctoral dissertation. Massachusetts Institute of Technology. <http://hdl.handle.net/1721.1/27939> (1984).

24. Dershowitz, W. S. & Einstein, H. H. Characterizing rock joint geometry with joint system models. *Rock. Mech. Rock. Eng.* **21**, 21–51 (1988).
25. Welch, M. J., Lüthje, M. & Oldfield, S. J. *Modelling the Evolution of Natural Fracture Networks*. Springer International Publishing; **10** <https://doi.org/10.1007/978-3-030-52414-2> (2020).
26. Davy, P. et al. DFN, why, how and what for, concepts, theories and issues. In: *ARMA International Discrete Fracture Network Engineering Conference*. ARMA; 2018:D013S000R001. <https://onepetro.org/ARMADFNE/proceedings-pdf/DFNE18/DFNE18/D013S000R001/4090922/arma-dfne-18-0310.pdf> (2024).
27. WSP UK Limited. FracMan Energy Edition, Version 8.3. Published online 2024. <https://www.wsp.com/en-gb/services/fracman> (2024).
28. Bonneau, F., Henrion, V., Caumon, G., Renard, P. & Sausse, J. A methodology for pseudo-genetic stochastic modeling of discrete fracture networks. *Comput. Geosci.* **56**, 12–22 (2013).
29. Libby, S. et al. Grown Discrete Fracture Networks: a new method for generating fractures according to their deformation history. In: *Proceedings of the 53rd US Rock Mechanics/Geomechanics Symposium*. ARMA19–1559; 23–26. (2019).
30. Libby, S. et al. Exploring the impact of fracture interaction on connectivity and flow channelling using grown fracture networks. *Q. J. Eng. Geol. Hydrogeol.* **57**, qjieg2023-010 (2024).
31. Hodge, M. S. et al. Multiscalar 3D temporal structural characterisation of Smøla island, mid-Norwegian passive margin: an analogue for unravelling the tectonic history of offshore basement highs. *Solid Earth* **15**, 589–615 (2024).
32. Selvadurai, A. P. S., Boulon, M. J. & Nguyen, T. S. The Permeability of an Intact Granite. *Pure Appl. Geophys.* **162**, 373–407 (2005).
33. Hestnes, Å. et al. Constraining the tectonic evolution of rifted continental margins by U-Pb calcite dating. Published online 2023. <https://doi.org/10.1038/s41598-023-34649-z>.
34. Fossen, H., Khani, H. F., Faleide, J. I., Ksienzyk, A. K. & Dunlap, W. J. Post-Caledonian extension in the West Norway-northern North Sea region: The role of structural inheritance. In: *Geological Society Special Publication*. Geological Society of London. **439**, 465–486 <https://doi.org/10.1144/SP439.6> (2017).
35. Oda, M. Permeability tensor for discontinuous rock masses. *Géotechnique* **35**, 483–495 (1985).
36. Sanderson, D. J. & Nixon, C. W. The use of topology in fracture network characterization. *J. Struct. Geol.* **72**, 55–66 (2015).
37. Nyberg, B., Nixon, C. W. & Sanderson, D. J. NetworkGT: a GIS tool for geometric and topological analysis of two-dimensional fracture networks. *Geosphere* **14**, 1618–1634 (2018).
38. Lei, Q. & Wang, X. Tectonic interpretation of the connectivity of a multiscale fracture system in limestone. *Geophys. Res. Lett.* **43**, 1551–1558 (2016).
39. Sibson, R. H. Structural permeability of fluid-driven fault-fracture meshes. *J. Struct. Geol.* **18**, 1031–1042 (1996).
40. Tartaglia, G. et al. Time-constrained multiphase brittle tectonic evolution of the onshore mid-Norwegian passive margin. *GSA Bull.* **135**, 621–642 (2023).
41. Holdsworth, R. E. et al. Natural fracture propping and earthquake-induced oil migration in fractured basement reservoirs. *Geology* **47**, 700–704 (2019).
42. Faulkner, D. R. et al. A review of recent developments concerning the structure, mechanics and fluid flow properties of fault zones. *J. Struct. Geol.* **32**, 1557–1575 (2010).
43. Nortje, G. S. et al. New faults v. Fault reactivation: implications for fault cohesion, fluid flow and copper mineralization, Mount Gordon Fault Zone, Mount Isa District, Australia. *Geol. Soc. Spec. Publ.* **359**, 287–311 (2011).
44. Sibson, R. H. A note on fault reactivation. *J. Struct. Geol.* **7**, 751–754 (1985).
45. Blenkinsop, T. G. Relationships between faults, extension fractures and veins, and stress. *J. Struct. Geol.* **30**, 622–632 (2008).
46. Stephens, M. B. et al. Review of the deterministic modelling of deformation zones and fracture domains at the site proposed for a spent nuclear fuel repository, Sweden, and consequences of structural anisotropy. *Tectonophysics* **653**, 68–94 (2015).
47. Macente, A., Dobson, K. J., MacDonald, J., Wadsworth, F. B. & Vasseur, J. The evolution of paleo-porosity in basalts: reversing pore-filling mechanisms using X-ray computed tomography. *Transp. Porous Media* **145**, 697–717 (2022).
48. Roberts, D., Luneburg, C., Jin, D. & Kato, J. Utilizing a kinematic and mechanical modelling workflow to constrain fracture network characteristics: application to the Teapot Dome, Wyoming, USA. *J. Struct. Geol.* **159**, 104596 (2022).
49. Maillot, J., Davy, P., Le Goc, R., Darcel, C. & de Dreuzy, J. R. Connectivity, permeability, and channeling in randomly distributed and kinematically defined discrete fracture network models. *Water Resour. Res.* **52**, 8526–8545 (2016).
50. Davy, P., Le Goc, R. & Darcel, C. A model of fracture nucleation, growth and arrest, and consequences for fracture density and scaling. *J. Geophys. Res. Solid Earth* **118**, 1393–1407 (2013).
51. Walsh, J. J., Watterson, J., Heath, A., Gillespie, P. A. & Childs, C. Assessment of the effects of sub-seismic faults on bulk permeabilities of reservoir sequences. *Geol. Soc. Lond. Spec. Publ.* **127**, 99–114 (1998).
52. Selby, D. & Creaser, R. A. Direct radiometric dating of hydrocarbon deposits using rhenium-osmium isotopes. *Science* **308**, 1293–1295 (2005).
53. Bhullar, A. G., Karlsen, D. A., Backer-Owe, K., Seland, R. T. & Le Tran, K. Dating reservoir filling—a case history from the North Sea. *Mar. Pet. Geol.* **16**, 581–603 (1999).
54. Ohm, S. E., Karlsen, D. A., Phan, N. T., Strand, T. & Iversen, G. Present Jurassic petroleum charge facing Paleozoic biodegraded oil: Geochemical challenges and potential upsides, Embla field, North Sea. *Am. Assoc. Pet. Geol. Bull.* **96**, 1523–1552 (2012).
55. Matapour, Z. & Karlsen, D. A. Ages of Norwegian oils and bitumen based on age-specific biomarkers. *Pet. Geosci.* **24**, 92–101 (2018).
56. Palumbo, F., Main, I. G. & Zito, G. The thermal evolution of sedimentary basins and its effect on the maturation of hydrocarbons. *Geophys. J. Int.* **139**, 248–260 (1999).
57. Peron-Pinvidic, G. & Osmundsen, P. T. The Mid Norwegian - NE Greenland conjugate margins: rifting evolution, margin segmentation, and breakup. *Mar. Pet. Geol.* **98**, 162–184 (2018).
58. Watts L. M., Holdsworth R. E., Roberts D., Sleight J. M. & Walker R. J. Structural evolution of the reactivated Møre-Trøndelag fault complex, Fosen Peninsula, Norway. *J. Geol. Soc. Lond.* <https://doi.org/10.1144/jgs2022-139> (2023).
59. Goff, J. C. Hydrocarbon generation and migration from Jurassic source rocks in the E Shetland Basin and Viking Graben of the Northern North Sea. *J. Geol. Soc. Lond.* **140**, 445–474 (1983).
60. Georgiev, S. V. et al. Comprehensive evolution of a petroleum system in absolute time: the example of Brynhild, Norwegian North Sea. *Chem. Geol.* **522**, 260–282 (2019).
61. Khorasani, G. K. Factors controlling source rock potential of the Mesozoic coal-bearing strata from offshore Central Norway: application to petroleum exploration. *Bull. Can. Pet. Geol.* **37**, 417–427 (1989).
62. Ali A. *Basin Modelling: HC Generation Modelling of the Åre, Melke and Spekk Formations, Haltenbanken Area*. Master Thesis. University of Oslo, Accessed July 3, 2024, <http://urn.nb.no/URN:NBN:no-31313> (2012).
63. Wang X., Dove C., Dunne J. E., Gutierrez W. M., Westman M. S. *Stereological Interpretation of Rock Fracture Traces on Borehole Walls and Other Cylindrical Surfaces*. Doctoral dissertation. Virginia Polytechnic Institute and State University, Accessed December 5, 2023, <http://hdl.handle.net/10919/29105> (2005).

Acknowledgements

This research has been supported by the Research Council of Norway (grant number 319849). The authors would like to thank the WSP UK Edinburgh office for the assistance and guidance while completing this study. We thank the NGU colleagues for discussions and providing constructive input. All the colleagues from the University of Bologna and, in particular, the Deformation, Fluids and Tectonics (DFT) research team, are specially thanked for their continual support and encouragement. Haakon Fossen and an anonymous reviewer are thanked for their truly constructive inputs and feedback, which led to a much-improved version of the manuscript.

Author contributions

M.S.H. contributed to conceiving the study, collected the data, undertook the statistical analyses, modelling, and results validation, produced the figures and wrote the paper (original draft and editing). M.C. guided model production and contributed to the editing of the manuscript. J.K. performed funding acquisition and contributed to editing the manuscript. G.V. conceptualised the study, obtained funding, acted as PhD project supervisor, and contributed to the writing of the manuscript (original draft and editing).

Competing interests

The authors declare no competing interests.

Additional information

Supplementary information The online version contains supplementary material available at <https://doi.org/10.1038/s43247-025-02146-y>.

Correspondence and requests for materials should be addressed to Matthew S. Hodge or Giulio Viola.

Peer review information *Communications Earth & Environment* thanks Steven Laubach and Haakon Fossen for their contribution to the peer review of this work. Primary Handling Editor: Carolina Ortiz Guerrero. A peer review file is available.

Reprints and permissions information is available at <http://www.nature.com/reprints>

Publisher's note Springer Nature remains neutral with regard to jurisdictional claims in published maps and institutional affiliations.

Open Access This article is licensed under a Creative Commons Attribution 4.0 International License, which permits use, sharing, adaptation, distribution and reproduction in any medium or format, as long as you give appropriate credit to the original author(s) and the source, provide a link to the Creative Commons licence, and indicate if changes were made. The images or other third party material in this article are included in the article's Creative Commons licence, unless indicated otherwise in a credit line to the material. If material is not included in the article's Creative Commons licence and your intended use is not permitted by statutory regulation or exceeds the permitted use, you will need to obtain permission directly from the copyright holder. To view a copy of this licence, visit <http://creativecommons.org/licenses/by/4.0/>.

© The Author(s) 2025